



TECHNICAL ARTICLE

# Probabilistic Machine Learning Assisted Feature-Based Qualification of DED Ti64

SOUMYA NAG,<sup>1,4</sup> YIMING ZHANG,<sup>1</sup> SREEKAR KARNATI,<sup>1</sup>  
LEE KERWIN,<sup>2</sup> ALEX KITT,<sup>2</sup> ERIC MACDONALD,<sup>3</sup> DORA CHEUNG,<sup>2</sup>  
and NEIL JOHNSON<sup>1</sup>

1.—GE Research, Niskayuna, NY, USA. 2.—Edison Welding Institute (EWI) Buffalo Manufacturing Works, Buffalo, NY, USA. 3.—Youngstown State University, Youngstown, OH, USA. 4.—e-mail: Soumya.Nag@ge.com

Additive manufacturing usually involves the complex interaction of design, materials, and manufacturing, often resulting in long and cost-intensive iterative evaluation cycles. Therefore, it is critical for it to be aligned with the Materials Genome Initiative to develop, produce, and deploy high-throughput components. Recognizing a need, this study leverages a feature-based qualification (FBQ) methodology to decompose a complex structure by identifying critical performance-limiting features, for the purpose of reducing the cost and time of DED process qualification. A hybrid-physics-based multi-objective optimization tool was used to predict processing-structure-property relationships in thin-walled builds. The probabilistic ML models achieved targeted predictions with half the sample space when compared with conventional DOEs, while also being 37–50% more reliable with respect to regression tools with linear basis function. Although the current model developed is specific to Ti64 builds in a RPMi557 powder-feed DED machine, the FBQ methodology may be more universally employed to other material-modality combinations.

## INTRODUCTION

The flexibility of additive manufacturing (AM) processes, with ‘new, unlimited dimensions’ of manufacturing, allows for significant customization of material properties, geometry, and surface conditions through variation in process and processing conditions.<sup>1</sup> However, this flexibility has one notable drawback—the complex interaction of design, materials, and manufacturing often leads to long iterative evaluation cycles. All this also drives uncertainty about component performance of AM parts, leading to long product qualification times and costs.

Currently, it can take several years to go from part concept to production on mission critical additively manufactured components. This is incredibly prohibitive to the broad adoption of AM technologies for use in sustainment applications where cost and readiness are vital to the acquisition process. The AM product qualification timeline is comprised of

design engineering and supply chain substantiation and development, but the longest task in the timeline is process authentication. Process substantiation in the past has been an extremely iterative cycle of preparing builds, printing parts, post-processing, conducting dimensional inspection, material performance evaluation, and functional performance evaluation. Component performance includes both form and function—relative to requirements—during design, operation, and sustainment. That is, it needs to perform its intended function and also do so for a sustained and predictable period of life. Historically, performance prediction for traditionally manufactured components primarily relied on coupon testing from which design performance curves were constructed using various statistical measures and safety factors. This approach has been, and continues to be, costly. It’s clear that the conventional test-and-fit approach will not be cost-effective for designing or qualifying additively manufactured components. Also, in the same vein, developing the complex processing-

microstructure-performance understanding and relations is time consuming for the needs these components fulfill in current designs.

With the above argument in mind, it is clear that new methods and tools are needed by the AM community to reduce process substantiation time and cost, and increase the probability of successful transition to production. In the past, probabilistic methods and tools have been successfully used by General Electric (GE) to predict the performance of powder bed AM processes. The current approach using directed energy deposition (DED) additive modality leverages on similar probabilistic modeling tools and techniques to develop a performance catalog based on feature-based qualification (FBQ) methodology. The principle of this approach is to identify performance-critical features within a part, and subsequently conduct subscale feature-based design of experiments (DOEs) connecting build process parameters, additive characteristics, and material property relationships. The associated data is fed into a GE Bayesian Hybrid Modeling framework (GEBHM) in conjunction with Intelligent Design Analysis of Computer Experiments (IDACE) to build predictive models allowing for shortening the timeline and cost to go from design to manufacturing qualification. The schematic in Fig. 1 illustrates such an approach, where a thin-wall build feature within an High Pressure Compressor concept part has been identified for conducting multi-objective optimization on process-structure-property response surfaces.

The material of choice for this study is Ti-6Al-4V (Ti64), an alloy that has more than a 30% market share in the ever-growing field of additive

manufacturing (AM powder revenue is projected to reach \$2.1B in 2025).<sup>2</sup> Among the various market segments, the biggest drivers are healthcare and aerospace, where the yearly Ti64 powder production is estimated to be 600K lbs and 350K lbs, respectively. Among the various additive powder-based modalities, DED provides an opportunity to build parts at large volume, with build rates significantly faster than L/EB-PBF (Laser/Electron Beam Powder Bed Fusion) techniques.<sup>3</sup> Yet, to date, very few if any validated methodologies (aside from trial-and-error experimentation) exist to aid in predicting the performance of Ti-6Al-4V components built using high-throughput powder-blown DED-based additive manufacturing.

Using the above material-modality combination, the performance catalog and FBQ methodology does enable more efficient design of components targeted for DED production by providing the engineering community with a feature-based performance and property data tool. The approach leverages a single experimental trial to benefit a wide range of products and geometric features where the mechanical properties and microstructural characteristics can be readily predicted. Manufacturing engineers may employ the feature-based process when preparing a component build and use the FBQ methodology to define the qualification work scope, testing requirements, and acceptance criteria. Although the model developed in this body of work is based on, and limited to, static properties, broadly applying the methodology and tool will help reduce the time, effort, and cost to bring DED components to production.

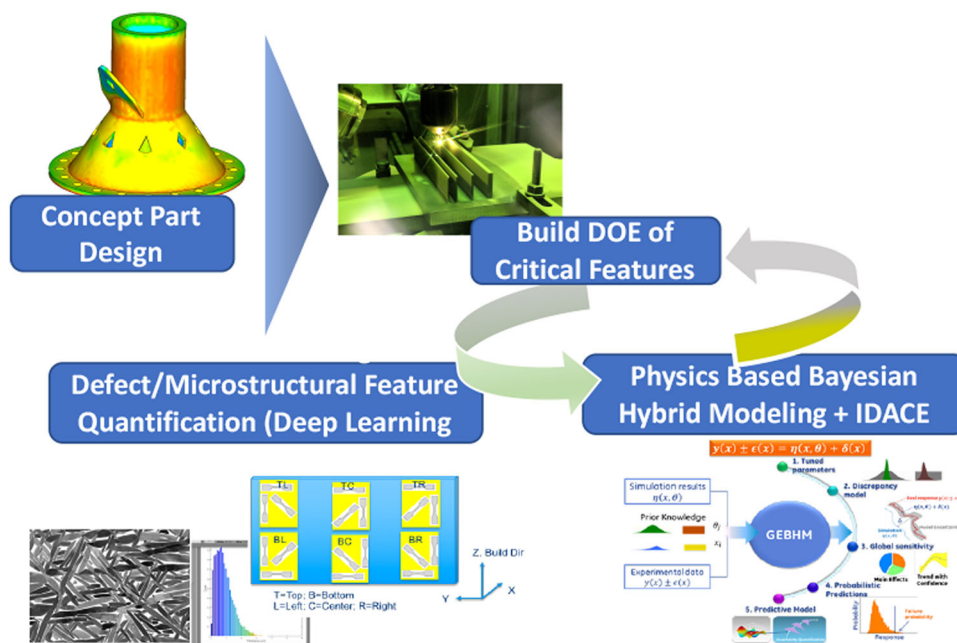


Fig. 1. Schematic of feature-based qualification methodology showing a concept part, selection of critical (thin wall) feature builds and using quantitative characterization and testing data to generate physics-based Bayesian hybrid models.

## MATERIALS AND METHODS

### Feature Selection

To achieve the overall program objectives and deliverables, a conceptual example component, representative of the aviation and aerospace industry and procedural guide/framework for feature-based decomposition was developed. In the current study, a concept part (Fig. 1), was designed to mimic a typical pressure case used in gas turbines. The design aspects are consistent with usual parts of this nature, such as the overhang angle of flanges or the included angle of holes and intersections. A 'feature' within the aforementioned concept part can be defined as a nominal geometric form, commonly named and used to characterize a shape, such as thin walls, rhombus or teardrop shaped holes, edges and overhangs. A feature can also be defined or classified as a result of build characteristics necessary to construct a physical shape, some of which are unique to additive manufacturing processes such as up-skin, or down-skin. From the operations perspective, there may be features within the component where stress levels are near the critical levels for the material's properties or where there is general concern or uncertainty about the result of an AM build strategy and parameters. Several features could be potentially identified from the concept part—though the current manuscript is focused on discussions around thin vertical wall features only.

### Powder Composition and Analyses

In the current DED-based effort, Ti-6Al-4V powders in the size range 45–105  $\mu\text{m}$  were used. Two different powder lots were procured for feature-based DOE (thin vertical wall) builds: Lot # 18-G416 and Lot # 192-G2021. The concept part was built using single recycled powder from Lot # 192-G2021, while the Lot # 18-G416 was used in thin vertical wall builds for validation trials. Each powder lot was subjected to standard procedures to obtain accurate chemical analyses as well as determine their physical characteristics like particle size distribution, flowability, and density (apparent and tap). See supplementary Tables S1 and S2 that compare the two lots of powder being used in this study.

As evident from the Tables, the two powder lots are very similar to each other with respect to flowability, apparent and tap density, as well as oxygen content. The major difference lies in the powder size distribution, where Lot # 18-G416 seems to have the size distribution peak skewed towards lower particle size. In terms of minor elemental additions, the nitrogen content for Lot # 192-G2021 is observed to be more than that found in Lot # 18-G416.

### Powder Blown DED Machine

The RPMI 557 additive manufacturing machine was used to construct all component and test builds in the current effort. The RPMi 557 machine is a laser, blown powder, directed energy deposition (LBP-DED) additive manufacturing process in which metal powder is injected into the focused beam of a high-power laser under an inert atmosphere of < 10 ppm of oxygen. The general equipment capabilities of this machine are listed below.

#### *Equipment Information*

- X/Y travel: (1524 mm)
- Z travel: (2133 mm)
- RT positioner—(610 mm diameter) (1000 kg capacity)
- 3 + 2 axis of operation
- 3 kW IPG YAG CW laser (5 modules)
- Powder feeders—dual (45  $\mu\text{m}$  → 150  $\mu\text{m}$  PSD)
- Shield/carrier gas—argon
- Glovebox environment—inert, < 10 ppm O<sub>2</sub>
- Nozzle angle—25 deg

### Build DOEs

The criteria for setting up build DOEs for the thin vertical wall feature was to (i) successfully build predetermined feature dimensions (length and height) of interest, (ii) explore as wide a range of build process parameters as possible which also determines the width of thin-wall structures, and (iii) employ different tool path strategies to fabricate similar build geometries.

The following is a deep dive into the rules that were set to generate this wide-net build DOE:

- Fully executed builds will have > 99% density.
- Vertical wall geometry
- Depending on build strategy and build parameter combinations, target thickness was in the range of 0.05" to 0.5". Thus, for different tool path strategies the final wall thickness (as function of bead width and step-over distance) was measured.
- To minimize buckling tendencies, the maximum thin-wall height and length were set up to be 6" and 10" respectively. Any vertical wall that was built to the abovementioned targeted dimensions was considered a success. Within the build DOE for certain build parameter/tool path strategies the wall builds were stopped at the onset of distortion, cracks or underbuilding events. The walls that had a final build height of < 4" were considered failed builds.

Several parameters per wall thickness were targeted by varying:

- Process parameters: beam diameter, laser power, powder feed rate, and travel speed
- Tool path strategy: single bead (S), triple bead (T), and contour and hatch (C+H) patterns as illustrated in Fig. 2. In each case, the outer blue and green arrows designate beam traversal vectors during outer contour and inner bulk builds, respectively.
- The resulting number of sample builds was a tradeoff between final wall sizes, deposition rate, and change overs, and best effort for time allocation.

For all builds the deposition head stand-off distance was fixed at 0.375" based on nozzle geometry. As evident from the compilation in Table I, a wide range of laser power, beam diameter and travel speed (referred here as scan velocity) were intentionally adopted so as to cast a wide-net DOE for this study.

### Sample Extraction, Post-Build Heat Treatment and Test Plan

After completion of thin-wall builds, the next step was to extract and evaluate the static tensile behavior of these features. The extraction strategy was

devised such that one can evaluate the effect of (i) build parameter and build strategy on thin vertical walls, (ii) post-processing (machining of as-built surface, hot isostatic pressing and subsequent heat treatment), and (iii) test location (tensile sample extraction zone and orientation with respect to build direction). A multi-layered approach was adopted to correlate build parameter, post-processing, and specimen extraction methodology with the ensuing build characteristics, zone-based distribution of defects and microstructural features, and site-specific physical and mechanical properties.

The top-down approach involves dividing each of the as-built vertical walls into 6 unique panels, as shown in Fig. 3. Thus, in the case of a fully successful thin vertical wall build (wall dimensions that are 10" long × 6" tall), individual panels that are ~ 3.25" × 3.25" define unique zones along height (top/bottom) or length (left/center/right) directions. The left and center of each vertical wall (TL, TC, BL and BC panels) were subjected to pre-cut up stress relief treatment and will hence forth will be designated as "AB + SR." In contrast the right side of each wall (TR and BR panels) were subjected to post-cut hot isostatic pressing (HIP-ed) and heat treatments. These will be addressed as "HIP + HT."

The main goal for such an arrangement was to:

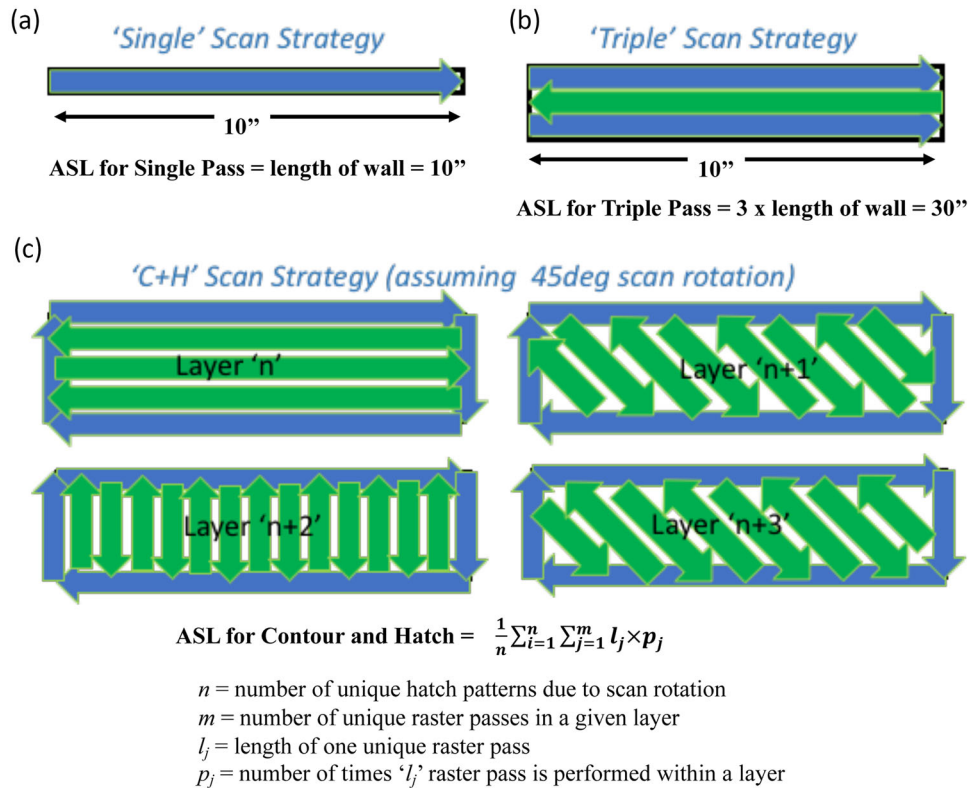


Fig. 2. Schematic showing the (a) single pass, (b) triple pass, and (c) contour and hatch (C+H) tool path strategies that were adopted in the current study. In each case, the blue and green arrows designate beam traversal vectors during outer contour and inner bulk builds, respectively. Also, a calculation of average scan length (ASL) per layer of thin-wall build is included for each tool path strategy (Color figure online).

**Table I. A compilation of thin vertical wall builds where different build parameters are associated with the actual number of tensile tests conducted for each build**

Build ID # (as per conditions)	Laser power (W)	Beam diameter (in)	Tool path strategy	Mass feed rate (g/min)	Scan velocity (in/min)	# of tensile specimens (as-built + stress relieved)	# of tensile specimens (HIPed + heat treated)
1	400	0.03	Single	4.8	40	9	4
2			Single	5.2	40	11	12
3			Triple	4.8	40	8	4
4			C+H	4.8	58	12	6
5	550	0.04	Single	5.2	30	12	6
7			Triple	5.2	40	8	4
8	625	0.04	C+H	5.2	50	12	6
9	1250	0.1	Single	7.5	30	10	5
12			Triple	7.5	40	12	6
13			C+H	7.5	52	12	6
10	1425	0.1	Single	7.5	30	10	5
11			Single	9.5	45	5	3
14	2180	0.1	Single	10.2	26	18	17
15			Triple	10.2	35	12	6
16			C+H	10.2	41	12	6
Total # of tensile specimens	163	96					

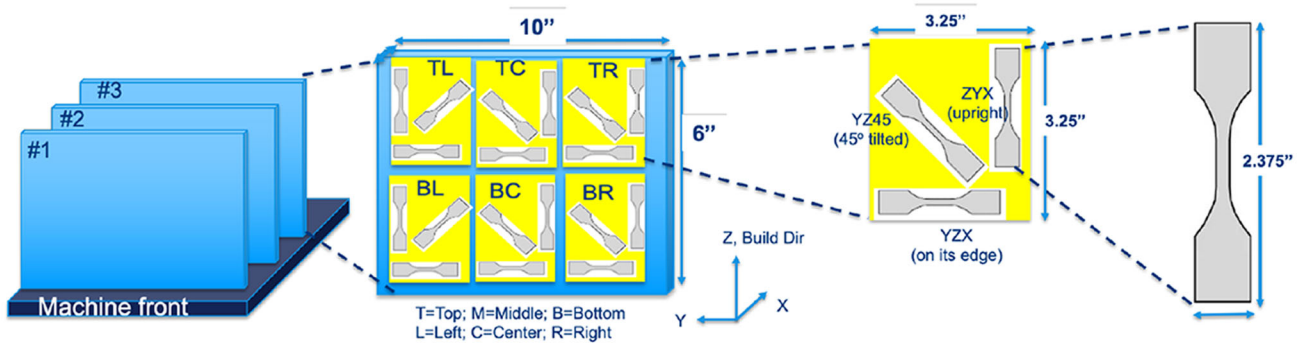


Fig. 3. Schematic illustration detailing the tensile coupon extraction from a plain wall feature.

- Compare the properties and microstructures of stress relieved panels on left and center locations of the thin vertical walls.
- Compare properties and microstructures of stress relieved panels on the left side and fully HIP'ed and heat-treated panels on the right side of the thin vertical walls.

The post-processing thermal treatment of the builds is a critical step to prevent cracking of builds (part integrity) as well as achieving the desired defect density and microstructural feature size—both important aspects for obtaining optimized properties. The goal was to determine the effect of build parameters on the microstructure and properties of DED Ti-6Al-4V: the data from which would be used to train a Bayesian hybrid model (BHM). Thus, the first step was to select a heat treatment that would provide enough stress relief (SR) to minimize

distortion during build removal from the substrate plate, but at the same time minimize influence on microstructure and as-built properties. To achieve this, a 50% SR was selected by using the stress relief nomograph provided in ASM International's Materials Properties handbook on titanium alloys. Subsequently, HIP treatment at 15 ksi and 1650 °F temperature (~200 °F below the beta transus of Ti-6Al-4V) was performed on a subset of panels to ensure closure of as-built porosities. Conducting the HIP at sub-transus temperature ensured that we do not grow the prior beta grains while dissolving the as-built alpha phase. The post-HIP cooling rate was carefully monitored to prevent subsequent coarsening of alpha laths. The actual stress relief, HIP, and heat treatment schedule was compiled (see supplementary Table S3).

Figure 4 shows a subset of thin vertical walls that went through an iterative cycle of (a) initial build

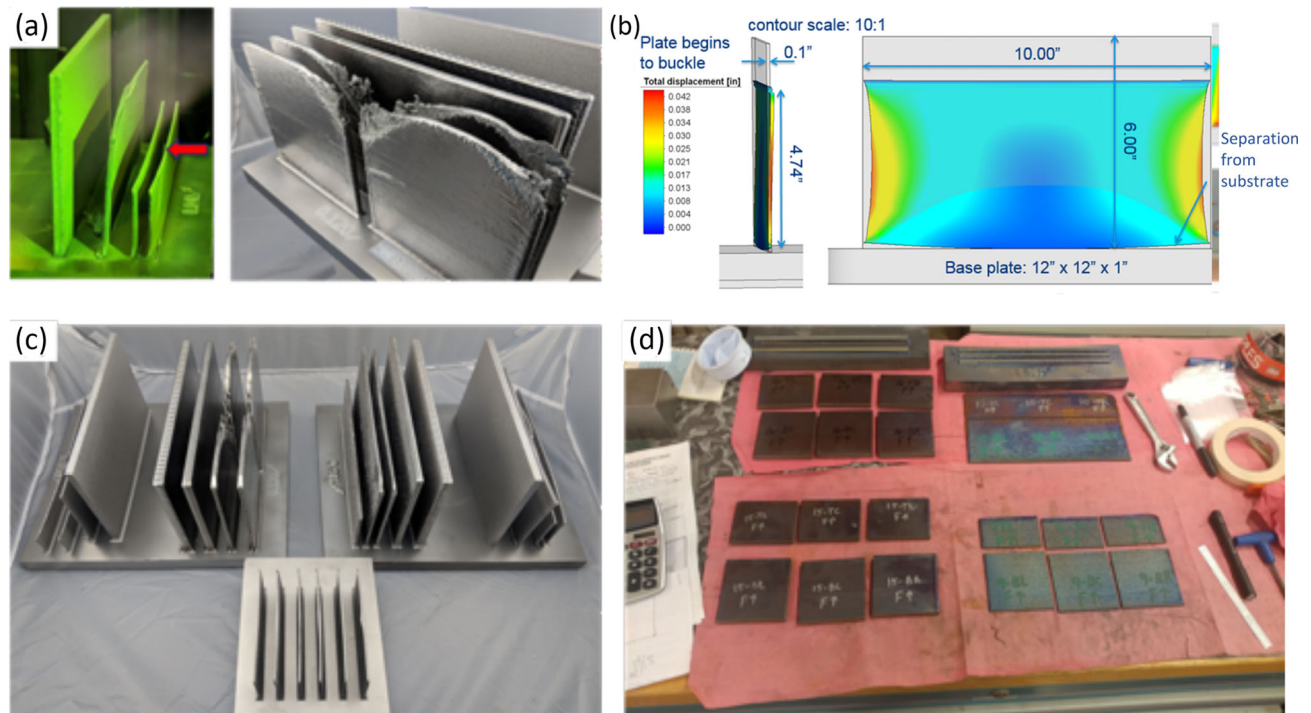


Fig. 4. (a) Initial build trials of thin-wall builds, and (b) corresponding simulation that exhibits underbuilding and buckling effects. (c) Fine tuning the build parameters to successfully build thin vertical walls. (d) Smaller panels, as per schematic in Fig. 3, were cut up for microstructural evaluation and testing.

trials that were partially successful, while other builds failed due to warpage, underbuilds and cracks, (b) conducting stress simulations using commercial software (Simufact Engineering GmbH) to identify high stress zones, (c) fine tuning build parameters to result in > 90% successful builds with 15 uniquely different combinations of build parameter, build strategy, and wall width, and (d) finally sectioning of fully built walls into distinct panels for characterization and testing.

Dog-bone shaped flat tensile coupons were extracted from each of these panels at three different orientations with respect to the build direction, as shown in Fig. 3. As per this figure, 'ZYX' denotes sample extraction along the vertical direction (parallel to build direction), while 'YZX' and 'YZ45' denote samples being tested at horizontal (perpendicular to build direction) and inclined at 45 degrees with respect to build direction, respectively.

The nominal thickness of the sheet tensile specimen was kept similar to the as-built thickness of the thin-wall builds. The broad face of the flat tensile specimen was machined for approximately 1/3 of the extracted specimens, while the rest of the samples were tested with inherent as-built surface roughness. A summary of the testing procedure followed for testing dog-bone tensile samples for thin-wall builds is listed below.

- All tests were conducted at room temperature (75 °F) according to ASTM E8 specifications. An

extensometer was set to measure 4D elongation (4 times the gage width).

- Initial testing was conducted with a strain rate of 0.005 +/- 0.002 in/in/min through 0.2% offset yield. Once yield had been reached, the tests were completed to failure at a crosshead speed of 0.250 in/min.

### Zone-Based Characterization

Understanding the microstructural hierarchy of as-built and post-processed Ti-6Al-4V alloy is an important step towards its accurate 2D feature quantification. For this, images at various magnifications were compiled to capture various microstructural length scales of interest. The overarching objective was to obtain quantitative descriptors of as-built walls and post-tested tensile specimens that could be incorporated into the Bayesian hybrid model (BHM). Table II shows a summary of quantitative measurement techniques used for estimation of various physical properties and microstructural and defect analyses, coupled with associated measurement objectives and quantifying units of measure.

### Bayesian Hybrid Modeling

The current physics-based predictive framework includes the following features: (i) forward prediction with cross validation, (ii) global sensitivity analyses, (iii) inverse prediction and optimization,

**Table II. A summary of various techniques employed for analytical measurement and quantitative characterization**

	Measurement technique	Measurement objective	Units of measurement
Physical properties	Surface profilometer Archimedes principle	Surface roughness Build density	Microns g/cc; % density
Defect analysis	Optical mosaic and image analysis	Area fraction of defects	% of evaluated cross-sectional area
	3D nano CT	Maximum defect size Total porosity Largest pore size	Microns % by evaluated volume Millimeters
		Location of max pore size from wall surface	Millimeters
Microstructural descriptor	Optical montage	Prior beta grain width	Microns
	X-ray diffraction	Weight fraction of alpha and beta phases Lattice parameter of alpha phase	% by weight 'c/a' ratio of hcp alpha phase
	Electron backscattered diffraction (EBSD)	Build layer thickness Average texture (index J)	Microns per layer Multiples of uniform density
	High resolution SEM and image analyses	Alpha lath length and width Thickness, aspect ratio and volume frac. of alpha phase	Microns Microns Microns, % of evaluated volume

and (iv) intelligent data addition to reduce uncertainty.

The forward modeling was performed with Bayesian hybrid modeling (BHM), based on the Los Alamos National Lab implementation, which has been extensively developed by GE Research over the past decade.<sup>4</sup> BHM is a Bayesian calibration technique that enables calibration of low-fidelity simulation data, building emulators of either of these two data types, uncertainty quantification, and updating/adapting as more data becomes available.<sup>5-7</sup> It is especially suited for sparse data which are expensive to compute or observe and has been shown to be computationally efficient and robust for noisy data. BHM is based on auto-adjusted weights (i.e., non-parametric) which can handle non-linear datasets better than linear regression, and has also been enhanced with Bayesian inference for training of the model parameters which enables reliable uncertainty estimations for prediction. BHM is rooted in the Gaussian process (GP) which has been well demonstrated for efficient modeling of sparse datasets with noise. GP is a non-parametric model which is a linear combination of the dataset with auto-weights according to the spatial distribution. GP is more robust compared with neural networks and more capable of handling non-linearity compared with linear regressions. The GP surrogate model follows the form as shown in Eq. 1, where  $m(x)$  is the mean function at input  $x$  and  $k(x, x')$  is the covariance function. A common covariance function is the squared exponential kernel as in Eq. 2, where  $\beta$  is the length scale parameter for each input

dimension,  $\sigma^2$  captures the amount of data variance captured by the model, and  $\lambda^2$  quantifies the amount of variance captured by the residuals.

$$y(x) \sim GP(m(x), k(x, x')) \quad (1)$$

$$k(x, x') = \sigma^2 \exp\left(-\beta(x - x')^2\right) + I\lambda^2 \quad (2)$$

The BHM training process is fully Bayesian with Markov chain Monte Carlo (MCMC) which reduces the risk of over-tuning and enables effective uncertainty propagation. The GP surrogate generated from the GEBHM framework ensures high accuracy and fast prediction for highly non-linear and non-monotonic design spaces for uncertainty quantification and propagation, when a limited number of model simulations are available. The forward modeling is evaluated with 10-fold cross validation, which means that the training dataset is divided into 10 out of which 1 is used as the testing set and the remaining 9 are used as the training set. Thus, 10 sets of BHM models are built in sequence and validated using their respective training set, respectively.

Global sensitivity is part of the BHM capability based on the variance analysis.<sup>8</sup> Variance based global sensitivity analysis investigates how the uncertainty of a mathematical/simulation model of a system can be divided amongst the different uncertain inputs and their interactions. Here, the model of a system could also be an actual experiment that studies the system with point-wise evaluations. Such methods rank the inputs according to

the following criterion: if the true value of the uncertain parameters is known, then how much variance in the output can be reduced? Hence higher reduction in variance means that the output is more sensitive to that input. Here it is important to distinguish between polynomial regression-based analysis of variance (ANOVA) methods and the generic variance decomposition methods. ANOVA methods are also variance decomposition methods but specialized for only polynomial models. Sobol indices are defined as in Eq. 3 where  $Y$  is the system response and  $X$  is the input variable.

$$S_i = \frac{\text{Var}[E(Y|X_i)]}{\text{Var}(Y)} \quad (3)$$

The Sobol indices are known to be good descriptors of the sensitivity of the model to its input parameters, since they do not suppose any kind of linearity or monotonicity in the model. The above expressions for Sobol indices can be estimated directly with a model that is relatively inexpensive to evaluate. However, in reality, simulation models or physical experiments are rarely inexpensive. In such problems, meta-models such as Gaussian processes are of use as they can be evaluated millions of times to estimate the Sobol indices given in Eq. 3. Even though meta-models replace the black box simulation models, computation of Sobol indices by directly sampling a meta-model quickly becomes computationally expensive as the number of dimensions increase. Thus, a specialized method has been adopted for the Gaussian process to calculate the semi-analytical solutions of the sensitivities.<sup>9</sup>

Inverse/backward predictions are formulated upon the developed surrogate models. Forward prediction calls on developed models to predict properties from given process variables. The input variables and predicted properties would change accordingly to accommodate multiple features for different application conditions. The input variables should be within the suggested range to avoid extrapolation beyond the experimental results. Prediction distribution including mean and standard deviation will be provided from forward predictions. The standard deviation estimates prediction uncertainty and could be used to adjust the mean value to acquire conservative prediction. The backward prediction, built upon the forward prediction, is a multi-objective constrained optimization process to search for the desired input variables by iteratively calling on forward prediction. This reverse prediction is formulated in a probabilistic manner leveraging the prediction distribution. For optimization of identified outputs, expected improvements are adopted as the objective within the identified range, as in Eq. 4, where  $EI$  stands for expected improvement,  $f^*$  is the optimum from the current dataset,  $\mu(x)$  and  $\sigma(x)$  are, respectively, the mean and standard deviation of BHM prediction at  $x$ , and

$\Phi(\bullet)$  and  $\phi(\bullet)$  are the cumulative distribution function and probability density function of the standard normal distribution, respectively. For prediction at specific output values, maximum likelihood estimation (MLE) is calculated to locate the unique set of input variables. For this, a popular genetic algorithm is selected for the iterative search after setting the objectives.

$$EI(x) = (f^* - \mu(x))\Phi\left(\frac{f^* - \mu(x)}{\sigma(x)}\right) + \sigma(x)\phi\left(\frac{f^* - \mu(x)}{\sigma(x)}\right) \quad (4)$$

After model development with an initial dataset, usually steps are taken to refine the same in terms of reducing the model uncertainty. Thus, GE's own Intelligent Design and Analysis of Computer Experiments (IDACE) tool is adopted for data addition.<sup>10</sup> IDACE takes the stochastic prediction from BHM and ranks the candidate points based on acquisition function.<sup>10,11</sup> Multiple types of acquisition functions are available within IDACE and maximum uncertainty for model refinement is adopted. In the current framework, IDACE is fully integrated with BHM which allows for fast and efficient navigation in high dimensional spaces by interrogating and updating the emulator in regions that stochastically minimize uncertainty. It performs adaptive design of experiments in an iterative manner which could make most use of the limited experimental budget to maximize the expected gain of models. The uncertainty information computed from the models is used to guide the placement of new points or optimal data distribution in the design space. It enables effective design space exploration and builds high-quality models with a minimum number of required additional simulations. The new points are selected iteratively to optimize the acquisition function (ranks the value of candidate points). Then evolutionary algorithms are adopted to determine the points corresponding to optimal acquisition functions. In summary, the critical features of IDACE include (1) multi-objective, constrained optimization based on the expected improvements of hypervolume in a probabilistic fashion, and (2) model refinement which reduces the prediction uncertainty of BHM models with data addition which could proceed in a greedy fashion or batch-wise.

## RESULTS AND DISCUSSION

### Data Assimilation

In the first round of sample extraction and testing, more than 200 samples were evaluated using 16 unique build parameters, as shown in Table I. As discussed earlier, roughly a third of these were tested under fully HIP-ed and heat-treated conditions, while the rest were only stress relieved. Also, a half factorial DOE scheme was



adopted to extract the testing response of machined (ground) vs as-built (unground) surfaces on the broad face of flat tensile specimens.

Post-characterization, the entire set of physical, material and mechanical property data was assimilated. This assimilation was necessary to perform a preliminary analysis as well as serving as an input to developing the Bayesian hybrid model (BHM). The assimilation process involved associating every individual measurement to its appropriate specimen fabrication, sourcing, treatment, and testing parameters. Every specimen that underwent characterization was traced using a unique specimen identifier. Using this identifier, an organized spreadsheet was constructed where each row was used to represent a specimen and its attributes. The columns were used to organize the various specimen attributes and characterization results. This spreadsheet was used for the purpose of preliminary analyses and BHM development.

From the assimilation layout, the input process variables contain categorical variables and multiple feed speed parameters. For modeling purposes, there was benefit in transforming the categorical variables to numerical variables. Similarly, selecting the feed speed that carries the most significance to the fabrication process was essential in minimizing the total number of variables.

Among input variables, one of the most crucial categorical variables is the tool path strategy that is depicted in Fig. 2. The three strategies considered in this study have substantial differences. To quantify these differences, a new continuous variable, average scan length, was defined. The average scan length is a measure of the average distance traveled by the laser in each layer. In the current study, the thin vertical wall feature was the same among the three different tool path strategies, namely single (S), triple (T) and contour and hatch (C+H) passes. The average scan length (ASL) calculation and values used for the three strategies are shown in Fig. 2. In the case of the C+H strategy, the scan length calculation was limited to the hatch raster, where  $n$  is the total number of unique hatch patterns created due to the rotating hatch angle,  $m$  is the number of unique raster passes in a given layer,  $l_j$  is the length of one of the unique passes and  $p_j$  is the number of times this raster pass is performed in a given layer.

It is to be noted that the average scan length variable is most influenced by the hatch-hatch spacing parameter. While calculation of the scan length is relatively simple for forward prediction-based model generation, for backward prediction, the scan length that is generated as an output needs to be associated with the three different tool path strategies. For example, if the value were in the range of 10" (which is the actual length of the thin-wall builds), then the predicted strategy would be single pass. Similarly, if the value were in the range of 30" (which is 3 times the length of the thin-wall

build), the predicted strategy would be triple pass. Any larger number that is predicted in the output column may be associated with C+H tool path strategy. In this case, the scan length equation in Fig. 2, may be used to numerically solve the actual hatch-hatch spacing. Thus, the hatch-hatch spacing may be correlated based on the bead width and the strategy election is based on the scan length value.

Again, to minimize the list of input variables and to only consider those with physical significance, a new variable named scan speed was defined. For build strategies where hatch speed and contour speed were both available, scan speed was set to the value used to deposit the bulk of the build. For example, in the triple pass strategy, in each layer, the two exterior passes are performed at contour speed and one interior pass is performed at hatch speed [as indicated by blue and green arrows in Fig. 2b, respectively]. Therefore, in this case, the scan speed was equated to contour speed. Similarly, in the case of C+H scan strategy the scan speed was equated to hatch speed, as the majority of the build incorporated hatch patterns (Fig. 2c). It is to be noted that for the builds, the ratio of contour speed to hatch speed was chosen to be 0.775.

## Mechanical Test Results

Due to the large number of parameters considered in this study, a thorough statistical analysis such as a multi-factor ANOVA analysis was not feasible. Identifying and estimating the statistical influence of the process parameters is challenging. However, such an analysis was not the intention behind this portion of the study. The chosen process parameters were expected to span a large portion of the viable process domain. These parameters were expected to produce quantifiable differences in the material outcome and performance. As observed in Fig. 5, the as-built additively manufactured tensile bars exhibited better yield strength and tensile strength than conventional as-cast Ti64 (baseline data as obtained from the Titanium handbook).

As discussed earlier, a total of 16 unique process parameters (Table I) were used to fabricate the wall feature builds. The first order analysis was aimed towards evaluating success regarding producing near fully dense material, as well as understanding variation in performance. While a wide range of variation was captured, the sources causing this variation needed to be identified. Thus, data segmentation based on known sources of variation such as tensile specimen surface condition (as-built vs machined), and orientation of tensile loading direction relative to build direction (as-built material is expected to be anisotropic) was also performed. The statistical significance of influences from these factors was assessed through analysis of variance (ANOVA) study.

The box plots in Fig. 5a, compile the tensile data from all the thin vertical wall builds. Here all the

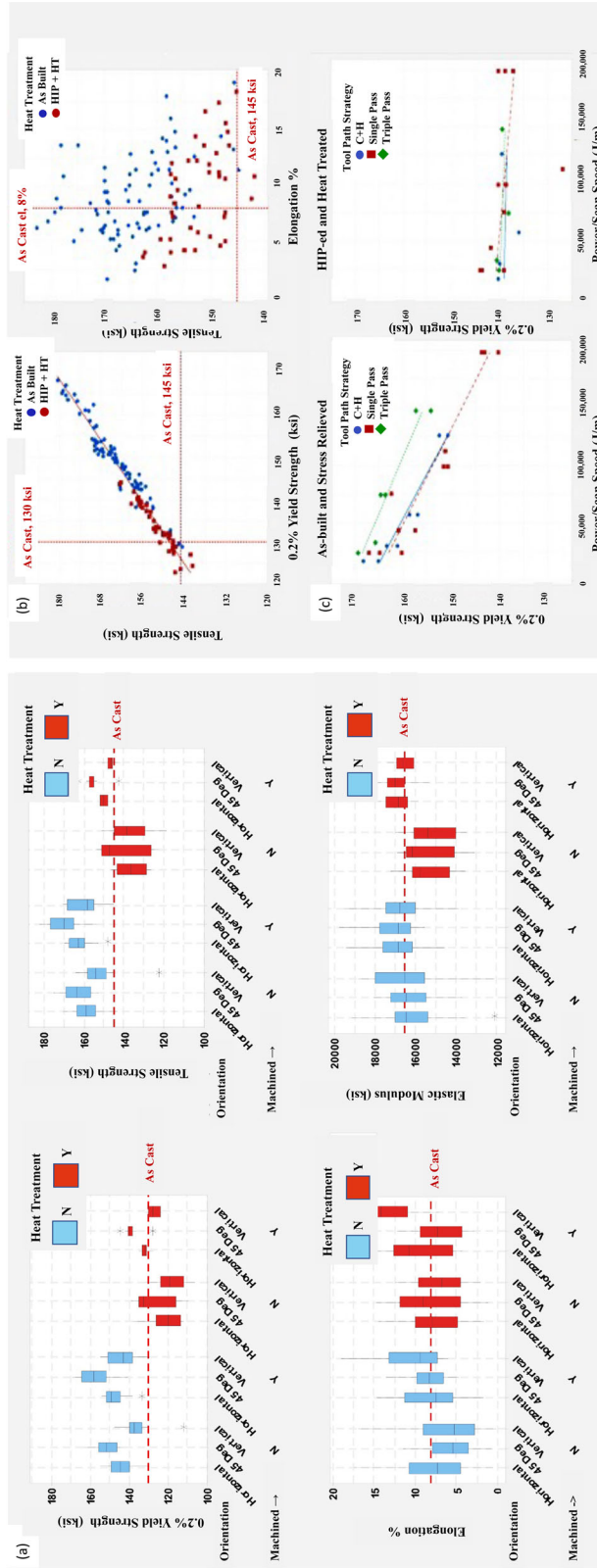


Fig. 5. (a) Box plots of tensile property measurements segmented by heat treatment condition, testing orientation and specimen grind condition. Subset of tensile data showing (b) tensile strength gathered from fully machined tensile specimens as a function of heat treatment condition, and (c) yield strength with increasing linear energy density for as-built and heat-treated specimens.

blue boxes represent samples that were stress relieved only (“*AB + SR*”, as mentioned above). Similarly, all red boxes indicate samples that were HIP-ed and heat treated (“*HIP + HT*” as mentioned above). From Fig. 5a, the anisotropy in strength can be realized from the trends in yield strength and tensile strength values. This anisotropy in strength was observed to exist even after heat treatment. Also, the differences in yield and maximum strength measurements with varying test orientations were observed to be statistically significant. Overall, within a given test orientation, the median strength measurements from specimens with the as-built surface condition (Machined = N in Fig. 5a) were observed to be slightly lower than specimens with the fully machined surface condition (Machined = Y in Fig. 5a). This difference in strength could be attributed to the difficulty in measuring the cross-sectional area of specimens with the as-built surface condition and the influence of surface roughness. The variation in %elongation was not as apparent as it was in the strength performance. No significant differences were found under this analysis. With regards to the Young’s modulus, the variation in scatter with heat treatment was most apparent. This variation in stiffness with heat treatment can be seen clearly between fully machined specimens (Machined = Y in Fig. 5a). It is to be noted that within this analysis, some of the measurements were also flagged as outliers if they were at least 1.5 times the interquartile range from the edge of the box.

### Correlation Among Tensile Properties

To benchmark the performance of the additively manufactured material against commercially sourced material, correlation plots relating tensile and yield strength, and tensile strength, and elongation were charted. It is to be noted that for this analysis, only the data from fully machined specimens was considered. The correlation charts are shown in Fig. 5b. The reference lines in the chart pertain to as-cast mean performance reported in the ASM Titanium handbook. Among the quadrants created by the reference lines, the top right quadrant pertains to the region where the performance is superior to cast material. From a strength standpoint, the majority of the data from both as-built (“*AB + SR*”) and HIP & aged (“*HIP + HT*”) were observed to be above the as-cast material. Also, a linear correlation was observed between the tensile and yield strength performance. Upon HIP and heat treatment a downward shift along the trend line was observed. The as-cast values from the handbook was also observed to be in close vicinity of the trend line. With regards to tensile strength and elongation, no apparent trends were observed. However, a good fraction of additively built Ti64 was observed to have inferior ductility the compared with as-cast conditions. This observation was true

in the cases of both as-built (“*AB + SR*”) and HIP & aged (“*HIP + HT*”) conditions. Also, for a given range of strength, a wide scatter in elongation was observed.

### Influence of Energy Input

Variation in energy input is known to influence the fabrication and performance of AM material. As previously mentioned, a detailed multi-factor analysis to assess influence of varying energy input parameters is challenging. However, insights into variation and statistical significance of process parameters are still possible. To assess the influence of energy input, linear energy density, the ratio of the power over scan speed was considered. Again, only the tensile data from fully machined specimens were considered. The data was also segmented by the tool path strategy and tensile gage orientation. Figure 5c is the variation in yield strength of fully machined specimens which were sampled with a tensile test orientated at 45° relative to the build direction. For the as-built (“*AB + SR*”) material, the drop in the yield strength with increasing energy input is apparent. However, post-HIP and heat treatment (“*HIP + HT*”) the yield strength appears to level out. These observations were also true for specimens with test orientation along and perpendicular to the build direction. Finally, the trends were identical for the observed ultimate tensile strength numbers.

### Impact of Build Parameters on Defects and Microstructure

Careful evaluation of defects and microstructure in as-built and post-processed Ti64 thin-wall builds exhibited a tremendous influence of build parameters, namely the linear energy density and build strategy. A few important findings are elucidated here. Figure 6a, b, c, and d is a compilation of the x-ray based 3D nano-computed tomography (CT) inspection process used to inspect and identify defects such as cracks and porosity either on the surface or within the bulk of vertical wall builds. Sample coupons from different locations of each wall build were examined so as to obtain a high signal-to-noise ratio. The center of each coupon was imaged at 6.5  $\mu\text{m}/\text{pixel}$  spatial resolution using the microfocus tube of an industrial nano CT scanner (Vtomex M 300). For this, an x-ray beam with 180 kV accelerating voltage and 120  $\mu\text{A}$  filament current was used (200 nm focal spot and 0.3 s exposure/frame). The data was reconstructed, and the volume rendered using a filtered back-projection method using a proprietary tool, DATOS™. The Volume Graphics Studio Max (v3.2.5) Easy Pore module was used to quantify and visualize porosity within the samples. After the analysis was completed, a map of defects was generated in 3-dimensional space. Key metrics such as location coordinates, maximum dimension, volume, surface area, and distance from the nearest

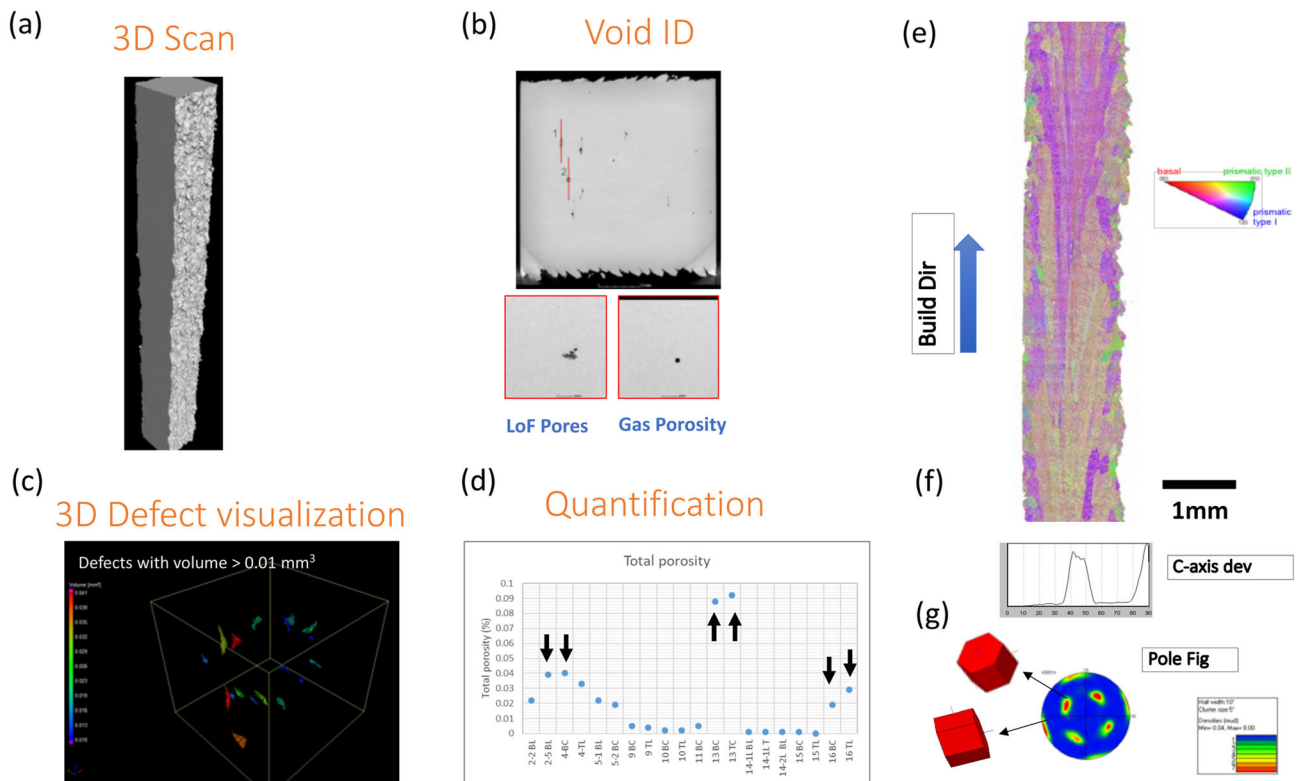


Fig. 6. A workflow for (a) 3D CT scan of a thin vertical wall build, followed by (b) identification, (c) visualization, and (d) quantification of lack of fusion and gas voids. The specimens built with C+H build strategy clearly show relatively high porosity %. Electron back scattered diffraction analyses of as-built thin vertical wall showing (e) inverse pole figure map along build direction, and corresponding (f) c-axis deviation map and (g) pole figure plot exhibiting predominantly 45-degree orientation of alpha laths with respect to build axis.

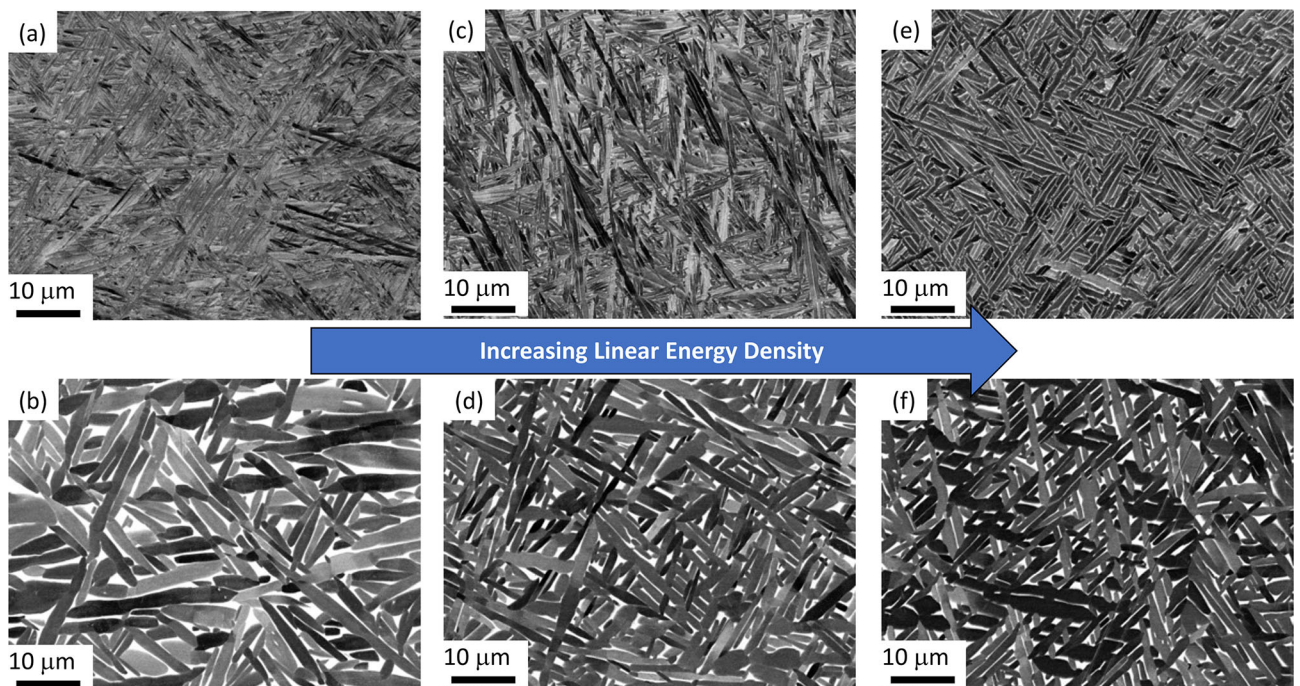


Fig. 7. Microstructure of Ti64 thin walls built with (a-b) low, (c-d) medium and (e-f) high linear energy density (laser power/scan velocity). (a), (c) and (e) are in as-built and stress relieved condition, and (b), (d) and (f) are in HIPed and heat-treated state.

edge were obtained for each defect. An overall percent porosity of all defects obtained from this analysis clearly showed that contour and hatch (C+H) build strategies (black arrows in Fig. 6d) had the highest amount of as-built porosity.

Electron backscatter diffraction (EBSD) analyses were performed on mounted and polished samples to determine the preferred crystallographic orientation of alpha phase which is a combined effect of as-built (liquid to solid beta phase) texture and variant selection process during beta to alpha solid-state phase transformation. A quantitative measure of texture was determined using MUD (multiples of uniform density) value, which is equivalent to the probability of finding a certain crystallographic orientation of alpha phase. MUD values from alpha grains with c-axis orientations at 45° and 90° relative to the build direction were obtained. Also, J-index notation was used to obtain a unique number representing the average degree of texture observed within a specimen. Usually, J-index ranges from a value of 1 (corresponding to a completely random fabric) to infinity (a single crystal fabric—ideally anisotropic). Thus, higher J-index value was indicative of greater extent of texture within a probed area. Figure 6e, f, and g is a compilation of alpha phase inverse pole figure (IPF), c-axis deviation and pole figure (PF) maps of thin and thick wall builds, as observed along wall width. The images clearly show a preferred crystallographic orientation of alpha phase (45-degree with respect to build axis) for thin-wall builds.

Apart from defect variation, the microstructure of Ti64 is greatly influenced by the build parameters, especially linear energy density or LED (corresponding to the yield strength and tensile strength values, as discussed in the previous segment). Figure 7 is a compilation of Ti64 microstructure obtained from similar regions of as-built (“AB + SR”) and post-processed (“HIP + HT”) thin-wall builds. Figure 7a shows a microstructure which is nearly 100% martensitic from an as-built and stress relieved vertical wall, built with the lowest LED. It is well known that martensites in Ti64 are formed when the cooling rate is at its highest. Similarly, Fig. 7c and e exhibit as-built and stress relieved microstructures that were built with progressively higher LED input. It is clear that Fig. 7e shows a closer to equilibrium alpha/beta microstructure, which indicates that the cooling rate experienced during this build was much slower than in walls built with lower LED (Fig. 7a). Thus, in this compilation, the inverse effect of LED on cooling rate and in turn its influence on microstructural feature size is clearly demonstrated. The effect of this microstructure is also observed in the tensile property response, as mentioned above in Fig. 5c—with martensitic structures showing higher strength and lower ductility, while the closer to equilibrium alpha/beta structure exhibits relatively lower

strength and higher ductility. Interestingly, Fig. 7b, d, and f show the corresponding microstructures from low, medium, and high LED thin-wall builds in fully HIPed and heat-treated conditions. It is clear that in all cases the Ti64 alpha/beta microstructures represent an equilibrium alpha/beta microstructure. This is also reflected in the tensile property response in Fig. 5c. It is evident that the microstructural variation of HIPed and HT samples (“HIP + HT”) with the lowest LED (Fig. 7b) vs highest LED (Fig. 7f) input is much less than the difference between as-built and stress relieved samples (“AB + SR”) with corresponding LED inputs (Fig. 7a vs e). Even then, one has to keep in mind that the mechanistic influence of post-processing heat treatment that causes tempering of martensites in low LED builds (microstructural change from Fig. 7a to b) is likely quite different from coarsening of alpha laths in high LED builds (microstructural change from Fig. 7e to f).

### Probabilistic Bayesian Hybrid Model Generation

To balance between buildability and space coverage of the initial dataset, the design of experiments was planned in a hybrid fashion in which 12 builds were from DED experts and 3 builds were from space filling in nature. Space filling methods (e.g., Latin hyper-cube sampling) are typically used for design of experiments when no prior information is available. For the current analyses, input from 266 sets of tensile specimen test data were collected in a hierarchical manner. An individual BHM model was developed for each output to accommodate the varying dataset size and make most use of all the collected data. Three types of model were developed to explore the mapping between different categories of inputs. The first one was the processing-property (PP) model which mapped from process parameters (build and post-build history) to mechanical and physical properties. The second one was the processing-microstructure (PM) model which mapped from process parameters to quantitative defect and microstructural identifiers. The third model was the microstructure-property (MP) model, used to map from defects and microstructure to mechanical and physical properties. The BHM models were developed and evaluated for all three types of model and individual output. The global sensitivities for three distinct models are summarized in Table III. It is clear that the  $R^2$  varied noticeably between the outputs. Also, some outputs such as elongation % were more challenging to predict due to the lower  $R^2$  value. For all three models, an  $R^2$  larger than 0.5 was considered to be acceptable. An example of the coefficient of determination ( $R^2$ ) for yield strength in the processing-property (PP) model is shown in Fig. 8a. The associate global sensitivities (Fig. 8b)

**Table III.  $R^2$  values obtained from 10-fold cross-validation and assessment of Process-Property, Process-Microstructure, and Microstructure-Property models**

Model type	Categories	Quantities of Interests/Outputs	$R^2$	
Process to Property	Mechanical properties	Tensile strength (ksi)	0.82	
		0.2% yield strength (ksi)	0.88	
		Elongation (%)	0.16	
	Physical properties	Modulus (Msi)	- 0.03	
		Build thickness (in)	0.97	
		Bead width (in)	0.49	
		Density (g/cc)	0.24	
		Surface roughness-wall front (mils)	0.91	
		Surface roughness-wall back (mils)	0.94	
	Build information	Materials Weight (g)	0.68	
		Build time (mins)	0.89	
	Property to Microstructure	Defect analyses	Nano-CT based pore volume (%)	0.87
			Nano-CT based max defect length (micron)	0.97
Microstructural analyses		Texture via EBSD (J-index)	0.92	
		Alpha lath aspect ratio	0.73	
		Alpha lath thickness (micron)	0.98	
		Prior beta grain width (mm)	0.88	
		Volume fraction of alpha phase	0.93	
Microstructure to Property	Mechanical properties	Tensile strength (ksi)	0.58	
		0.2% yield Strength (ksi)	0.52	
		Elongation (%)	- 0.32	

exhibit their first order and second order dependencies on build parameter (laser power) and post-processing (HIP) steps.

Post-model generation, IDACE was adopted for selection of additional builds. These were selected in an iterative manner as constrained optimization to satisfy the two buildability models. The estimated uncertainty reduction is shown in Fig. 8c. Thus, as per IDACE recommendation, the addition of 4 data points (tagged as “IDACE” in Fig. 8d) was expected to reduce the model uncertainty by 40%. Along with this, 4 additional builds were also included, half for model refinement and the other half for model validation (tagged as “Expert” and “Expert\_validation” in Fig. 8d). Thus, Fig. 8d visualizes the first buildability model with the proposed additional builds, along with the existing dataset.

Validation results of the forward model are provided in Fig. 8e. The additional dataset was centered in a reduced range between 120 ksi and 150 ksi. The 95% prediction interval (PI) was conservative to include the prediction error as show in Fig. 8f. For industrial applications, it is critical for the system to maintain function even at the maximum design allowable. Therefore, conservative estimates were needed in addition to the mean values. The calculated conservative estimates as the lower 10th percentile are shown in Fig. 8f. The experimental validation resulted in < 10% difference between measured test values versus prediction values for yield strength and tensile strength. At the end, the BHM and regression were compared with a basic linear basis function (LR) evaluated with 10-fold cross-validation (not shown). It was

evident that the BHM was comparable or better than LR for the examined properties, ~37–50% more accurate for yield strength and tensile strength.

### Summary of Observations

The current study showcases feature-based qualification driven response surfaces connecting processing, structure, and properties of vertical thin-wall DED Ti64 builds. Some of the observations connecting defects and microstructure to AM processing and corresponding static property response is compiled below:

- **Process Map:** To be able to validate and deploy this methodology at a broader scale and scope, one has to understand the connections between energy input and the feature build itself. Thus, there was a significant effort to extract normalized process maps in terms of heat flow in, coupling build parameters and material addition, analogous to the study by Thomas et.al. for generating processing diagrams for the powder bed AM process.<sup>12</sup> The Eqs. 5 through 7 below show a methodology to use beam diameter of the incident laser beam (BD) to normalize laser power ( $q$ ), scan velocity ( $v$ ), and layer thickness ( $l$ ), respectively. Note that all material parameters like surface absorptivity ( $A$ ), thermal conductivity ( $\lambda$ ), thermal diffusivity ( $\alpha$ ), melt temperatures ( $T_m$ ), as well as substrate temperature ( $T_o$ ) were assumed to be constant. These are embedded as constant terms  $C_{qn}$  and  $C_{vn}$  in Eqs. 5 and 6, respectively. From the abovementioned normal-

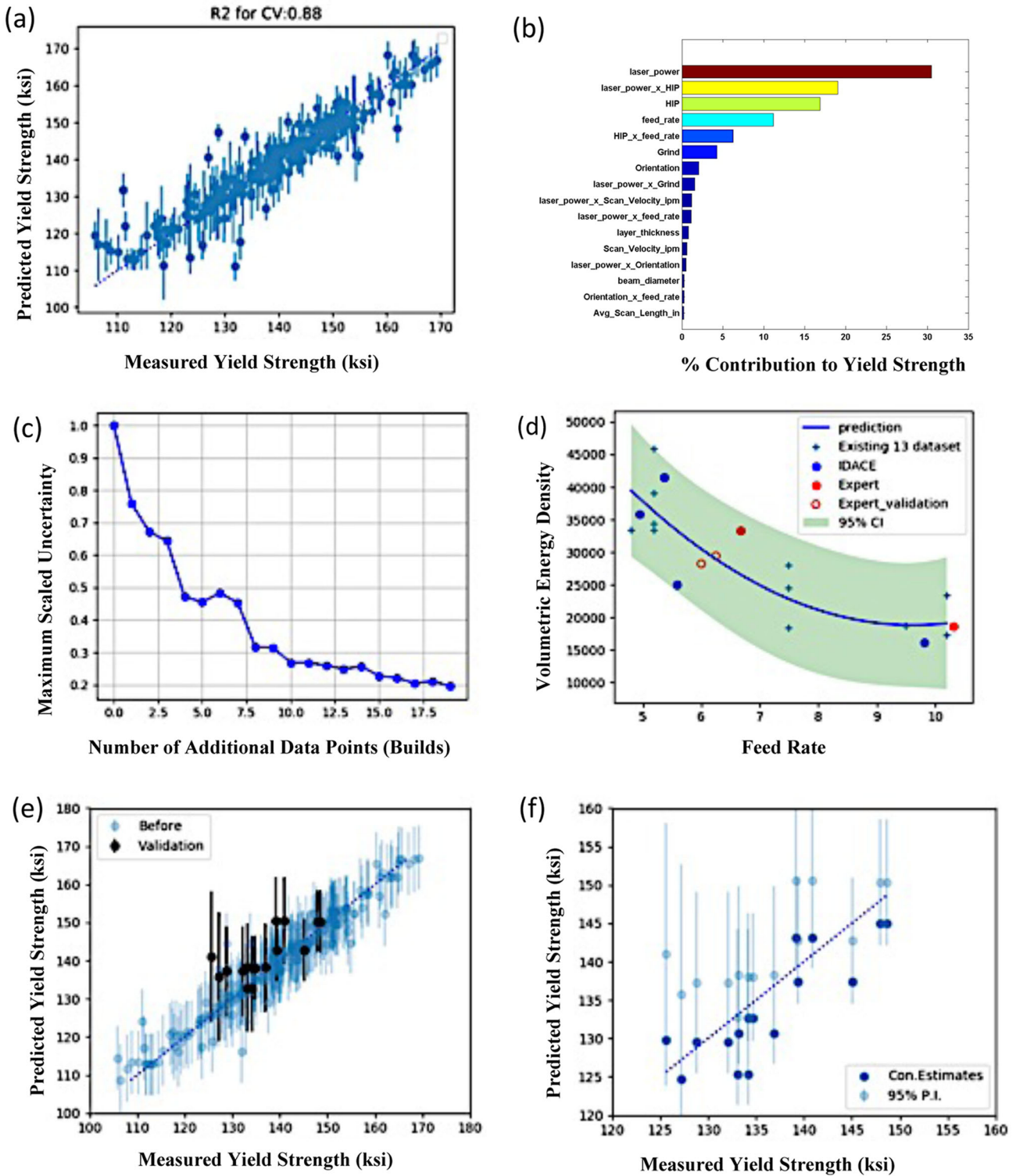


Fig. 8. BHM predictions for yield strength (a) cross-validation (b) global sensitivities. Data addition with IDACE (c) estimated uncertainty reduction with additional build, (d) buildability estimation for the additional dataset. Validation of the forward model (e) prediction with 95% prediction interval (f) conservative estimates with lower 10th percentile..

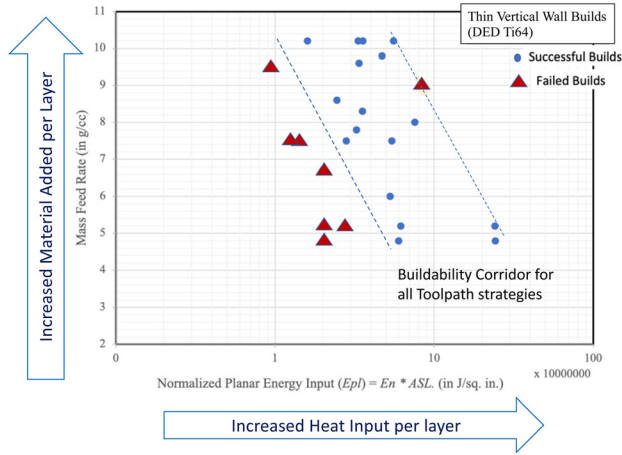


Fig. 9. A normalized planar energy input (volumetric energy density multiplied by actual laser track length) vs mass feed rate plot, showing a region of goodness for thin vertical wall DOE builds. All the builds within the ‘buildability corridor’ were successful, while the shaded region on the left demarcates builds that were not successful in terms of 6” wall height.

ized parameters ( $q_n$ ,  $v_n$ , and  $l_n$ ), one can calculate the energy required to melt a unit volume of material ( $E_n$ ), as shown in Eq. 8.

Taking this analysis a step further, one can determine the cumulative energy addition per unit layer stated as normalized planar energy input ( $E_{pl}$ ) by multiplying  $E_n$  with the average laser scan length, ASL (calculation shown in Fig. 2). Plotting  $E_{pl}$  vs mass feed rate (Fig. 9) shows a region of goodness within the thin-wall build process map. As indicated in Fig. 9, the red triangles are really the builds that were not successful in terms of 6” wall height, while all the other builds (blue circles) within the demarcated “buildability corridor” were successful. As one can see, this is a great way to bring all the thermal input factors together and help one guide towards future builds.

$$q_n = \frac{A * q}{\frac{BD}{2} * \lambda * (T_m - T_o) \alpha} = C_{qn} * \frac{q}{\frac{BD}{2}} \quad (5)$$

$$v_n = \frac{v * \frac{BD}{2}}{\alpha} = C_{vn} * v * \frac{BD}{2} \quad (6)$$

$$l_n = \frac{2 * l}{\frac{BD}{2}} \quad (7)$$

$$E_n = \frac{q_n}{v_n * l_n} = \frac{c_{qn}}{c_{vn}} * \frac{q}{v * l * \frac{BD}{2}} \quad (8)$$

- Effect of defects: Depending on the size of geometric discontinuity present in as-built material, the defects in Ti64 DED thin-wall builds may be broken down into two distinct groups—macro-scale and micro-scale defects.

Macro-scale defects are microns to millimeters in size and are associated with as-built surface roughness (function of bead width) and feature-based discontinuities of finite radius such as notches and divots (not discussed in this work). The results clearly point towards a tremendous sensitivity of macro-scale AM defects on tensile properties.

Micro-scale defects like lack-of-fusion voids, gas porosity, and cracks, seemed to have a subdued effect on properties, primarily due to very low volume fraction and smaller size of these defects. However, in some cases where the abovementioned macro-scale defects were reduced (e.g., fully machined samples), the large scatter observed in property response may be attributed to these micro-scale defects.

- Baseline microstructural influence: In the as-built state, the linear energy density or energy input (ratio of laser power and scan velocity) for a given feature with fixed build dimensions seemed to have the biggest influence on tensile strength and yield strength outcomes. This also had a strong influence on the associated Ti-6Al-4V microstructural attributes.

The ductility of such builds is a more complex phenomenon and its variations are also convoluted with build strategies and microstructural hierarchy (grain size, colony size, and alpha lath morphologies). If the tool path strategy, along with build dimensions, are held constant, the elongation trends are influenced by the conventional microstructural parameters, where cooling rate is the biggest influencer.

Post-build conventional hot isostatic pressing (HIP) does seem to equilibrate most of the abovementioned static property variations. However, the microstructural response to heat treatment is not well understood. This will be vital in understanding more microstructure sensitive properties like high/low cycle fatigue and fatigue crack growth, especially since the starting as-built microstructure and associated coarsening mechanisms are quite disparate.

## CONCLUSION

In this study, a feature-based qualification methodology was adopted to identify a thin vertical wall feature, extracted from a representative component (high-pressure compressor case) that was independently designed and additively fabricated without any optimization build strategies. Thin vertical walls of different (uniform) thickness, and tool path strategies were produced and served as a baseline and validation data. All the builds were produced using RPMI’s 557 equipment at Edison Welding Institute (EWI). A 3-kW IPG fiber laser was used as the energy source and the material of



choice was Ti-6Al-4V. Sixteen sets of unique processing conditions were used to generate a DOE and the builds were subjected to various post-processing steps including stress relief treatment, hot isostatic pressing (HIP), post-HIP aging and low-stress grinding. More than 250 mechanical tensile test samples were extracted and tested to generate a DOE based on the abovementioned variables. Samples were extracted at 3 different orientations (0, 45, 90 degrees with respect to the build direction) and from different locations throughout the build geometry (top vs bottom in terms of height, and left, center, and right in terms of length of the wall). Also, physical properties (density and surface roughness) of thin vertical wall features were determined. A select number of specimens were subjected to quantitative defect evaluation, and microstructural assessment. Analyzing the variation in performance, the process domain considered in the DOE resulted in a wide range of performance outcomes. The mechanical performance of the as-built material was found to be generally better if not similar to the as-cast material. This was true primarily for both yield and ultimate strength values. On the other hand, no discernable trends were found with the elongation data due to the large range of scatter. The AM material was found to exhibit significant anisotropy and heat treatment was found to be effective in minimizing it.

Using the abovementioned database, an independent Bayesian hybrid model (BHM) framework was generated as follows:

- Forward prediction of process parameters to tensile mechanical properties,
- Backward prediction from material (tensile mechanical properties) performance to process parameters,
- Microstructure to material performance (tensile mechanical properties).

This study successfully applied statistical design of experiments (DOE) for systematic planning of the DED builds. The initial DOE was produced with half the features from additive experts, and half from statistical methods. Then, intelligent data addition was adopted to balance between information gain and testing budget. Predictive models were built with  $R^2 > 0.5$  (cross validation) for the four features and different types of properties. Space-filling schemes were examined, and regression-based uncertainty reduction was used to improve modeling accuracy. A set of stochastic forward models were developed for multiple features to link various process parameters, microstructural characteristics and tensile mechanical properties. The forward models were evaluated with 10-fold cross-validation and compared with linear regression, showing noticeable improvements

(~33–57%). After establishing the forward models, robust backward models were generated for recommending desired deposition strategies and process parameters. The concept of robust optimization was introduced to account for the stochastic prediction from BHM. The backward modeling was rooted in a genetic algorithm to iteratively perform forward predictions which optimize the objective function based on stochastic predictions. Data addition for the purpose of model refinement with IDACE was used to adaptively obtain process variables to improve the model accuracy. All this was achieved with nearly half the resources used in terms of build and post-analysis cost and time, when compared with conventional half factorial DOE models.

As a final note, the current study made significant progress towards understanding a challenging subject for all AM processes, which is determining how part performance critical feature-based DOE can help generate and predict reliable processing-structure-property response surfaces (models). The tool offers the potential to reduce the number of iterations and cycle time to identify processing conditions that achieve a desired component and material performance. The currently developed modeling method can benefit various engineering, operations, and supply chain partners. This approach offers a tool to deconvolute complexities common to DED processes and also enables a pathway for accelerated adoption and deployment of DED technology.

#### ACKNOWLEDGEMENTS

This effort was performed through the National Center for Defense Manufacturing and Machining under the America Makes Program entitled Maturation of Advanced Manufacturing for Low-Cost Sustainment, and is based on research sponsored by the Air Force Research Laboratory under agreement number FA8650-16-2-5700. The U.S. Government is authorized to reproduce and distribute reprints for Government purposes notwithstanding any copyright notation thereon.

The authors would like to thank Mark Benedict and Thomas Broderick at AFRL, and Dave Siddle and Brandon Ribic at America Makes for their continued support and guidance throughout the course of this project. Furthermore, valuable insights and consultations for conducting stress simulations, DOE setup and Bayesian hybrid model creation is much appreciated from Ryan Hurley at EWI (now at DMG Mori), Genghis Khan, Changjie Sun and Sathya Raghavan at GE Research, and Chris Williams at GE Aviation. Author SN acknowledges sample preparation and characterization support from Anthony Poli, Jeremiah Faulkner, Ian Spinelli, Anjali Singhal, Rebecca Casey, Tracy Paxon and Yan Gao at GE Research, and John Sosa at MIPAR® Image Analyses.

### CONFLICT OF INTEREST

The authors declare that they have no conflicts of interest.

### SUPPLEMENTARY INFORMATION

The online version contains supplementary material available at <https://doi.org/10.1007/s11837-021-04770-3>.

### REFERENCES

1. Y. Bovalino and T. Kellner, GE:3D Printing Opens A 'New, Unlimited Dimension' For Manufacturing. <https://www.ge.com/news/reports/ge-3d-printing-opens-new-unlimited-dimension-manufacturing>. Accessed 15 January 2021.
2. SmarTech Analysis, Opportunities for Additive Manufacturing in Aerospace 2018–2023. <https://www.smartechanalysis.com/blog/page/3/>. Accessed 15 January 2021.
3. B. Dutta, S. Babu, B. Jared, *Science, Technology and Applications of Metals in Additive Manufacturing*, (Elsevier -1st ed, 2018) pp. 55-63.
4. S. Ghosh, P. Pandita, S. Atkinson, W. Subber, Y. Zhang, N. C. Kumar, S. Chakrabarti, and L. Wang. Preprint arXiv:2003.11939 (2020).
5. M. Kennedy, and A. O'Hagan, *J. R. Soc. (Series B)* 68, 425. (2001).
6. D. Higdon, M. Kennedy, J. Cavendish, J. Cafoe, and R.D. Ryne, *Siam J. Sci. Comput.* 26(2), 448. (2004).
7. D. Higdon, C. Nakhleh, and B. Williams, *Comput. Methods Appl. Methods Eng.* 197, 2431. (2008).
8. A. Srivastava, A.K. Subramaniyan, and L. Wang, In ASME Turbo Expo 2015: Turbine Technical Conference and Exposition. *American Society of Mechanical Engineers Digital Collection*. <https://doi.org/10.1115/GT2015-43693> (2015).
9. G. Li, and H. Rabitz, *J. Math. Chem.* 50(1), 99. (2012).
10. J. Kristensen, W. Subber, Y. Zhang, S. Ghosh, N.C. Kumar, G. Khan, and L. Wang, *Design Engineering and Manufacturing. Intech Open*. <https://doi.org/10.5772/intechopen.88313> (2019).
11. Y. Ling, K. Ryan, I. Asher, J. Kristensen, S. Ghosh, and L. Wang, *AIAA/ASCE/AHS/ASC Structures, Structural Dynamics, and Materials Conference*. (2018) <https://doi.org/10.2514/6.2018-0912>.
12. M. Thomas, G.J. Baxter, and I. Todd, *Acta Mater.* 108, 26. (2016).

**Publisher's Note** Springer Nature remains neutral with regard to jurisdictional claims in published maps and institutional affiliations.